International Journal of Hydrogen Energy 87 (2024) 1277–1287

Contents lists available at ScienceDirect

International Journal of Hydrogen Energy

journal homepage: www.elsevier.com/locate/he

Photoelectrolysis of glucose and fructose containing solution in PGM-free cells for hydrogen and valuable chemicals production

Claudio M. Pecoraro, Francesco Di Franco, Vittorio Loddo, Marianna Bellardita, Monica Santamaria *

Dipartimento di Ingegneria, Università degli Studi di Palermo, Viale delle Scienze Edificio 6, 90128 Palermo, Italy

ARTICLE INFO

Keywords:
Biomass partial oxidation
H_2 production
Photoelectrocatalysis
TiO_2 nanotubes
Pt-free electrodes

ABSTRACT

This study investigates the reforming of glucose and fructose by photoelectrolyis, employing TiO_2 NTs photoanodes for the selective oxidation of the carbohydrates and Ni foam as cathode. TiO_2 NTs with different structural features were grown on Ti felt via anodizing and annealing to promote their crystallization.

These electrodes were tested in aqueous solutions at three different pH values (i.e., 2, 7, and 12) both without and with the addition of biomass. When biomass was present, the hydrogen production rate increased, reaching faradic efficiencies (FEs) ~ 100% in spite of the use of undivided cell, allowing the simultaneous production of valuable partial oxidation compounds, such as gluconic acid (GA) and formic acid (FA), with FEs of 24% and 55% respectively, and overall quantum yields of 5.67% and 4.36% respectively. The photoanodes used demonstrated high mechanical and chemical stability under all the tested conditions, with electrode performance remaining consistent over time, allowing the reuse of the same electrode for a not limited number of runs after a mild cleaning step.The results demonstrated that this photoelectrocatalytic (PEC) process is promising for both biomass valorization and H_2 production.

1. Introduction

The depletion of fossil fuel reserves and the increasing environmental pollution have encouraged the scientific community's interest in renewable energy sources and, among them, H_2 stands out as a promising clean energy carrier [1–4]. In this context, an encouraging approach as an ideal and sustainable alternative to fossil resource utilization involves converting renewable biomass into H_2 and valuable chemicals [5–8].

Glucose and its isomer fructose, derived directly from cellulose, are the most abundant and renewable biomasses on Earth [9–11]. They can serve as precursors for producing ethanol, renewable diesel, and jet fuels, along with a wide array of biobased chemicals used as industrial feedstocks for bioplastics and hydrogen production [12–16]. Notably, the selective oxidation of these compounds to produce gluconic and formic acids is particularly appealing due to their industrial applications as platform chemicals [17–20].

Gluconic acid (GA) and its derivatives market values are expected to reach $1.9 billion by 2028 and find extensive use in the food, pharmaceutical, and detergent industries as flavoring and chelating agents [21, 22]. Moreover, formic acid (FA) serves as an energy carrier and is a crucial intermediate in chemical synthesis across industries ranging from chemical and agricultural to pharmaceutical, textile, and rubber. Its market value is expected to increase up to $4 billion in the next 10 years [23,24].

Various technologies involving high temperature and pressure conditions have been employed to produce GA and FA with low selectivity, difficult separation, pollutant emissions, and low yields, despite the use of expensive catalysts, oxidizing agents, and high energy consumption [25–31]. Therefore, there's a high demand for alternative methods for glucose and fructose conversion.

Photoelectrocatalysis (PEC) in aqueous solutions at ambient conditions emerges as a promising, environmentally friendly, and efficient alternative to chemical and enzymatic methods. PEC can be employed in biomass oxidation, H_2 production, and organic synthesis, combining renewable feedstock and green energy sources to concurrently produce building-block chemicals and clean fuel [32–39].

Within PEC systems, photoinduced electrons (e^-) and holes (h^+) can migrate through the applied electric field, with electrons moving to the cathode and holes to the surfaces of the photoanode. This charge

* Corresponding author.
E-mail address: monica.santamaria@unipa.it (M. Santamaria).

https://doi.org/10.1016/j.ijhydene.2024.09.124
Received 2 August 2024; Received in revised form 30 August 2024; Accepted 10 September 2024
Available online 14 September 2024

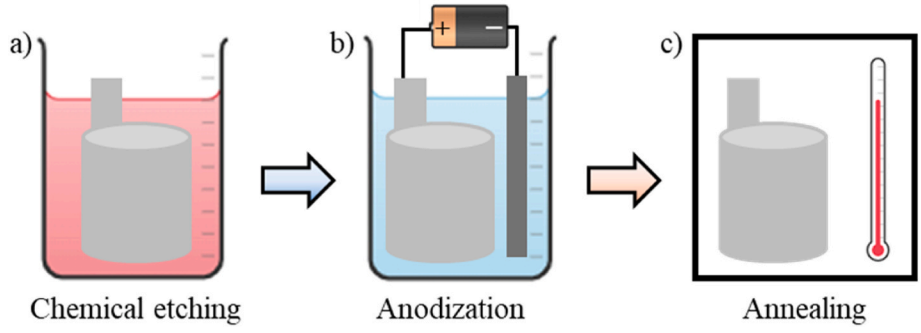

Fig. 1. Schematic illustration of the photoanode preparation process: a) chemical etching, b) anodization, c) annealing.

Table 1
Details of the bath composition, applied potential, and duration of the anodization process for the synthesis of the two samples used in the photoelectrocatalytic tests.

Sample	EG (%wt)	NH_4F (%wt)	H_2O (%wt)	Potential (V)	Time (min)
0.75% w	99	0.25	0.75	45	10
50%w	49.5	0.5	50	30	30

redistribution results in reduction and oxidation reactions occurring at these respective electrodes [40–42]. Despite extensive research on PEC systems for water splitting [43–45] and organic pollutant degradation [46–48], investigations into PEC oxidation of organic compounds remain relatively limited. Notably, the main challenge in PEC partial oxidation of organic compounds lies in achieving high selectivity towards desired products and high faradic efficiency (FE) [33,36,49–51]. As a photoanode, TiO_2 stands out as the leading choice in PEC systems due to its exceptional photocatalytic activity, high stability, scalability, cost-effectiveness, and non-toxic properties [52–56].

This study focuses on the anaerobic partial oxidation of glucose and fructose in an aqueous medium under mild temperature and pressure conditions to produce H_2 and high-value-added (HVA) products. Platinum group metal (PGM) free TiO_2 nanotubes (NTs) photoanode with different features (tubes wall thickness and distances among parallel tubes) and Ni foam cathode were used in the attempt to realize cost effective process with high stable materials. A photoelectrochemical investigation was carried out to get a complete description of the energetics of the semiconductor/electrolyte interface. To estimate FE toward HVA and H_2, GC and HPLC analyses were carried out as function of electrolyte pH.

2. Experimental

2.1. Electrodes preparation

TiO_2 nanotube photoanodes were fabricated by anodization (Fig. 1) [36,56,57].

Titanium fiber felt (Fuel cell store) with a thickness ranging from 0.2 to 0.3 mm was cut and etched for 2 s in a solution containing hydrofluoric acid (HF, Sigma Aldrich, purity 39.5%), nitric acid (Sigma Aldrich, purity 69.0%), and deionized water at a volume ratio of 1:1:3 (**Warning!** HF is a hazardous chemical that is toxic through inhalation, skin contact, and ingestion. All necessary precautions were observed during our experiments). Subsequently, they were sonicated in acetone and ethanol for 5 min each, followed by rinsing with deionized water and air-drying. Anodization was carried out in a two-electrode cell setup, with aluminum foil serving as the cathode in an ethylene glycol solution (EG, Aldrich, 99.8% anhydrous) containing NH_4F (Sigma Aldrich) and deionized water. TiO_2 nanotubes with different features were obtained by varying the anodization conditions, i.e., the composition of the anodization bath, time, and potential. The synthesis conditions are reported in Table 1.

Soon after the anodization step, both samples were annealed in air to 450 °C for 3 h to promote the crystallization of the TiO_2 nanotubes towards the anatase phase.

Commercial Ni foam (Goodfellow) was employed as the cathode.

2.2. Characterization

Scanning electron microscopy (SEM) images were captured using a FEI Quanta 200 ESEM microscope operating at 30 kV. X-ray diffraction (XRD) patterns of the photoanodes were obtained at room temperature utilizing a PANalytical Empyrean diffractometer equipped with a PIXcel1D detector operating at 40 kV and 40 mA, utilizing CuKα radiation, and with a 2θ scan rate of 3°/min.

Raman spectra were acquired using a Raman Microscope coupled with a Leica DMLM microscope. The laser was focused onto the sample through a 5× magnification lens to achieve an analyzing spot diameter of approximately 50 μm, with a maximum laser power of 133 mW. Only 10% of the maximum power was utilized, reduced by holographic filters (three for each sample). Spectra were recorded using a 532 nm laser coupled with a 2400 lines per millimeter grating, resulting in a spectral resolution of 0.5 cm^{-1}. Each measurement comprised two accumulations.

For the photoelectrochemical measurements, the TiO_2 nanotubes photoanode served as the working electrode in a three-electrode cell configuration, with a Pt wire as the counter electrode, and an Ag/AgCl/saturated KCl reference electrode. A 0.1 M ammonium biborate tetrahydrate (ABE, $(NH_4)_2B_4O_7 \cdot 4H_2O$; Sigma Aldrich), was employed as the electrolyte. The UV–vis Xenon lamp, with a power of 450 W, was employed. Its light was directed to a monochromator to enable selective wavelength irradiation of the sample surface through the quartz window of the cell. The electrode potential was regulated by a versastat potentiostat. To obtain the photocurrent spectra (i.e., photocurrent vs wavelength) by applying 0.5 V vs Ag/AgCl, the resulting current was directed to a two-phase lock-in amplifier to separate the photocurrent from the total current circulating in the cell. A mechanical chopper was utilized to halt irradiation at a predetermined frequency, specifically 13 Hz. Photocurrent spectra were reported in the text as photocurrent yield (Q_{ph}). This yield was calculated by considering the relative photon flux of the light source at each wavelength, reflecting the efficiency of the lamp-monochromator system.

Mott-Schottky (M − S) analysis was conducted under dark conditions by varying the applied potential from 1 V to −0.7 V vs. Ag/AgCl with a sinusoidal modulation of the applied potential of 10 mV amplitude and a frequency of 1 kHz.

Thermodynamic and kinetic aspects of the partial oxidation of glucose (Sigma-Aldrich) and fructose (Sigma-Aldrich) were investigated via cyclic voltammetry (CV) in a 0.5 M Na_2SO_4 (99% Sigma-Aldrich), both in the absence and presence of 0.1 M of biomass. Cyclic voltammetry measurements were conducted by employing a Parstat 4000

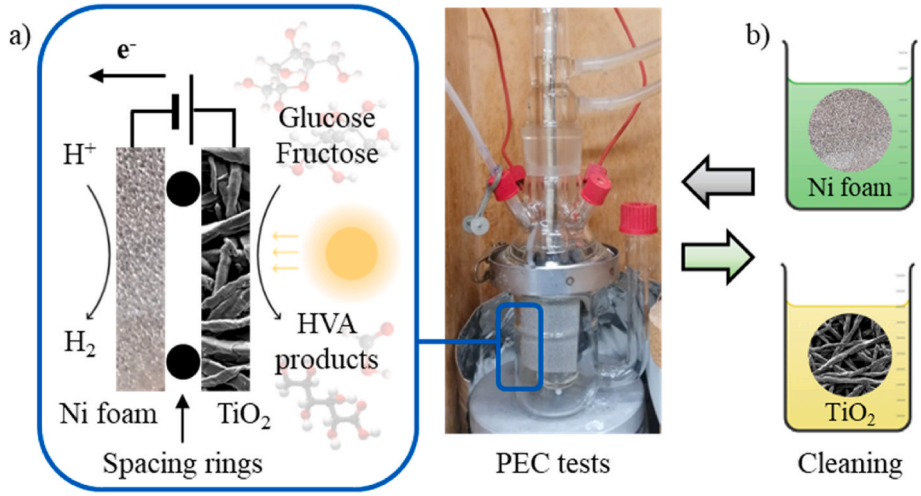

Fig. 2. a) Image of the PEC cell used, and the corresponding schematic illustration. b) Schematic representation of the electrode cleaning process.

potentiostat within the voltage range of 0–1.9 V vs RHE, utilizing a three-electrode cell configuration with Pt mesh serving as the working and counter electrode, and Ag/AgCl/sat. KCl as the reference electrode. A scan rate of 5 mV/s was employed. For the sake of comparison, CVs were plotted using the Reverse Hydrogen Electrode (RHE) potential, as described in Equation (1)

$$E_{RHE}\ (V) = 0.198 + 0.059\ pH + E_{Ag/AgCl} \quad (1)$$

where $E_{Ag/AgCl}$ is the working potential.

Electrochemical Impedance Spectroscopy (EIS) measurements were conducted using a Parstat 4000 potentiostat equipped with an Impedance Analyzer connected to the cell. Impedance spectra were recorded over the frequency range of 100 kHz to 0.1 Hz at 25 °C, applying 1 V between the photoanode and the cathode, and employing an AC amplitude of 10 mV. Before each measurement, the cell was allowed to stabilize for at least 15 min under irradiation. Data analysis and equivalent circuit fitting were performed using VersaStudio and ZSimpleWin software.

2.3. Photoelectrocatalytic test

Photoelectrocatalytic experiments were conducted utilizing TiO_2 NTs as the photoanode, Ni foam as the cathode, and 0.5 M Na_2SO_4 as the electrolyte. A scheme of the experimental setup is reported in Fig. 2.The pH was adjusted to 2 or 12 using H_2SO_4 or NaOH, respectively, and a potential of 1 V was applied between the photoanode and the cathode for 3 h. Glucose or fructose concentrations were 0.1 M. The reactions took place in undivided glass cells (Fig. 2), employing a two-electrode configuration. As the light source, a 125 W medium-pressure Hg lamp emitting mainly near-UV light at a wavelength of 365 nm was used. The power density of the emitted light of 10 mW/cm^2 was measured by using a radiometer. Photoanode and cathode surfaces were 90 cm^2 (irradiated) and 180 cm^2, respectively. A Parstat 4000 (PAR) potentiostat equipped with Electrochemical Impedance Spectroscopy (EIS) capabilities was utilized to regulate cell potential and gather kinetic data for both anodic and cathodic processes.

Before each run, Helium was bubbled under stirring in the dark for 30 min within the biomass aqueous solution to eliminate oxygen from the system and saturate the electrode surfaces with the substrate. Subsequently, the reactor was sealed, and the lamp was turned on. During the reaction time, water was circulated in the reactor cooling jacket to maintain the room temperature within the reaction mixture.

The photoanode was subjected to reuse after sonication with acetone and water for 5 min each to eliminate any glycerol residues, while Ni foam was cleaned by sonication for 5 min in 1 M HCl and water.

Table 2
Electrons/holes exchanged in the half cell reactions reported in Equations (3)-6)

Compound	Chemical formula	Electrons/holes exchanged
Glucose/fructose	$C_6H_{12}O_6$	
GA	$C_6H_{12}O_7$	2
FA	CH_2O_2	2
Carbon dioxide	CO_2	4
Hydrogen	H_2	2

2.4. Analitycal tecniques

The detection and quantification of glucose, fructose, and reaction intermediates were conducted using a Thermo Scientific Dionex UltiMate 3000 HPLC, equipped with a Diode Array detector and a REZEK ROA Organic acid H^+ column. Analysis of gaseous species collected in the reactor headspace was carried out using an HP 6890 Series GC system, featuring a Supelco GC 60/80 CarboxenTM-1000 packed column and a thermal conductivity detector.

The faradic efficiency for GA, FA, CO_2, and H_2 was determined using Equation (2):

$$FE\ (\%) = \frac{Amount\ of\ product\ i\ formed\ (mol)}{\frac{Q\ (Coulomb)}{z\ F\ \left(\frac{Coulomb}{mol}\right)}} \quad (2)$$

where.

- i is the formed product
- Q is the circulated charge
- z are the electrons exchanged, that are equivalent to the number of holes reported in Table 2 considering the half-reactions in Equations. (3) - (6)
- F is the Faraday constant of 96,485 [Coulomb/mol]

$$C_6H_{12}O_6 + H_2O + 2\ h^+ \rightarrow C_6H_{12}O_7 + 2\ H^+ \quad (3)$$

$$C_6H_{12}O_6 + 6\ H_2O + 12\ h^+ \rightarrow 6\ CH_2O_2 + 12\ H^+ \quad (4)$$

$$C_6H_{12}O_6 + 6\ H_2O + 24\ h^+ \rightarrow 6\ CO_2 + 24\ H^+ \quad (5)$$

$$2\ H^+ + 2\ e^- \rightarrow H_2 \quad (6)$$

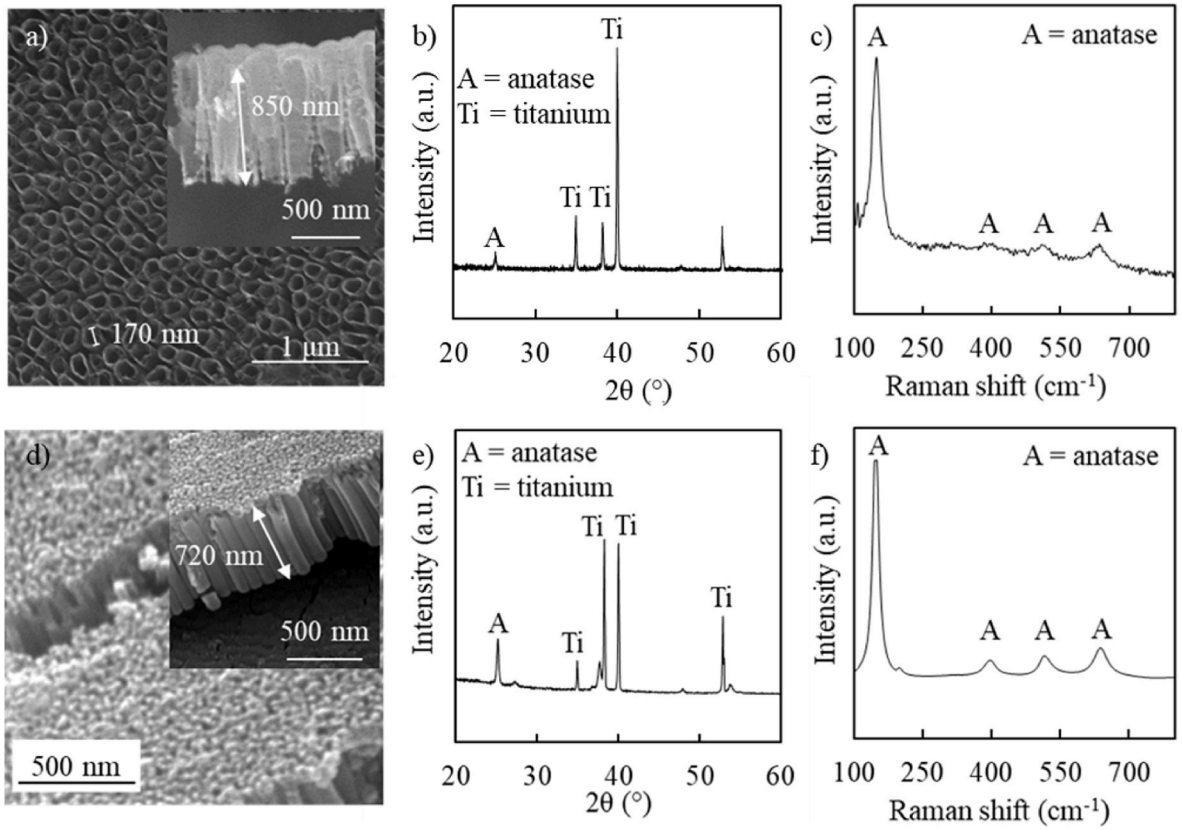

Fig. 3. SEM pictures, XRD patterns, and Raman spectra of (a–c) 50 %w NTs sample and (d–f) 0.75%w NTs sample.

3. Results and discussion

Fig. 3 compares the morphological features of TiO_2 NTs grown in ammonium fluoride containing ethylene glycol solution with 50% (Fig. 3a–c) and 0.75% of water (Fig. 3d–f), respectively, after thermal treatment at 450 °C for 3 h. The SEM micrographs distinctly reveal the achievement of a large array of TiO_2 NTs, wherein the average length is ~720 nm and 850 nm (inset of Fig. 3a and d). Notably, NTs grown in 50%w show thinner sharp walls with a large space among NTs, thus allowing a better contact and refreshment of the electrolyte during the photoeletrochemical process. These findings are consistent with earlier investigations [57].

XRD pattern for annealed TiO_2 NTs, reported in Fig. 3b and e, shows the reflections of anatase polymorph due to the crystallization of TiO_2 grown by the anodizing process, together with the reflections of titanium arising from the not anodized metal still present beneath the nanotube layers that allows an efficient electrical contact with the photoactive titania [58]. The presence of anatase is also confirmed by Raman spectroscopy. As shown in Fig. 3c and f characteristic bands of anatase polymorph are present at 144 cm^{-1}, 196 cm^{-1}, 397 cm^{-1}, 513 cm^{-1}, and 639 cm^{-1} [59].

A photoelectrochemical investigation aimed to gain information about the electronic characteristics of the photoanodes was carried out. The photocurrent spectrum, i.e. photocurrent as a function of the monochromatic irradiating wavelength, recorded under a constant bias polarizing the Ti/TiO_2 NTs layer electrode in a 0.1 M ABE aqueous solution at 0.5 V vs Ag/AgCl, is reported in Fig. 4a and shows that the photoresponse is high in the UV region due to the fundamental typical absorption of anatase TiO_2. Under the hypothesis of non-direct optical transitions, an estimation of the optical band gap value (E_g) was made by extrapolating to zero the $(Q_{ph} \cdot h\nu)^{0.5}$ vs $h\nu$ plot (Fig. 4b). The determined E_g is 3.15 eV, which is in line with the reported value for anatase (3.2 eV [57]). The photocurrent transients were measured by manually interrupting monochromatic irradiation (at $\lambda = 340$ nm), while applying a constant potential ranging from 0.5 to −0.5 V vs Ag/AgCl (see Fig. 4c). An anodic photocurrent was observed, confirming the n-type semiconductor behavior of the oxide, with the photocurrent reaching zero at approximately - 0.5 V vs Ag/AgCl. The zero photocurrent potential can be considered an estimate of the flat band potential, U_{fb}. This value agrees with that estimated by the M − S plot recorded at 1 kHz (Fig. 4d). It is important to mention that the flat band potential of TiO_2 NTs grown in water containing solution is slightly more positive than that estimated for NTs grown on ethylene glycol solution (i.e. −0.75 V Ag/AgCl [36]). This implies that the flat band potential is shifted toward the mid gap position. Additionally, the n-type behaviour of TiO_2 NTs is also confirmed by the cathodic photopotential recorded during the irradiation of the sample, as shown in Fig. 4e [60].

A preliminary electrochemical assessment was conducted to gather insights into the kinetics of glucose and fructose oxidation in 0.5 M Na_2SO_4 aqueous solution at different pH (i.e., 2, 7, and 12) within a potential range of 0–1.9 V vs. RHE. Fig. 5 illustrates the cyclic voltammograms obtained in solutions without and with biomass, utilizing a Pt mesh as the working and the counter electrode. At pH 2 (Fig. 5a), cyclic voltammogram reveals two oxidation peaks at 0.2 V, 0.7 V, and an oxidation current starting at 1.1 V vs. RHE in presence of glucose or fructose, with higher values being measured with fructose. According to the literature [61] in the case of glucose the first peak corresponds to the oxidation of the adsorbed hydrogen produced by chemisorption of the glucose molecule, that however does not poison the surface of the electrode, while the second peak is assigned to the oxidation of strongly adsorbed intermediate produced from the glucose oxidation in the first process. Only at high potential (namely 1.6 V vs RHE), oxygen evolution occurs suggesting that both glucose and fructose oxidation is more favourable. Notably, the OER is not significantly affected by the presence of the biomass, i.e., the current recorded at higher potential is comparable with and without biomass in the electrolyte.

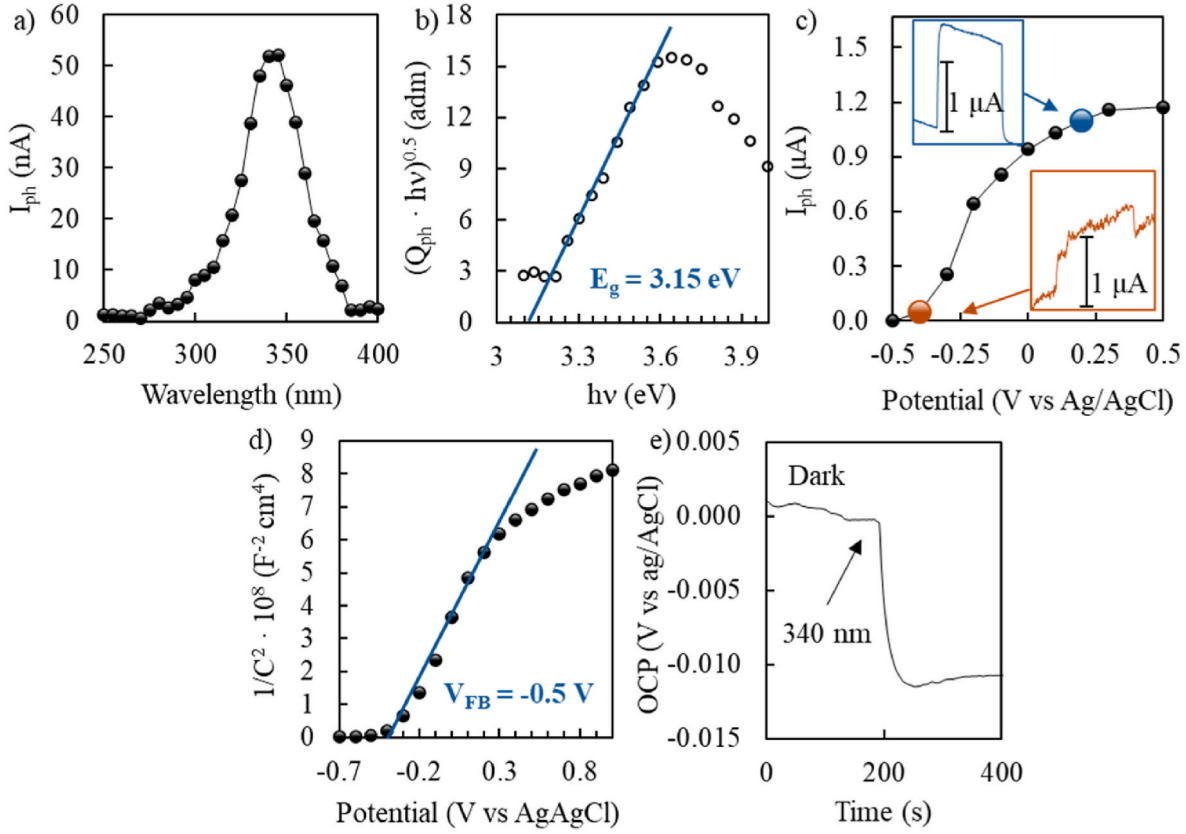

Fig. 4. a) photocurrent spectra recorded in a 0.1 M ABE aqueous solution at 0.5 V vs Ag/AgCl, b) respective $(Q_{ph} \cdot h\nu)^{0.5}$ vs hν plot for the E_g estimation, c) photocurrent transients under monochromatic light recorded at 340 nm and applied potential from 0.5 to −0.5 V vs Ag/AgCl, d) M − S plot recorded in a 0.1 M ABE aqueous solution at 1 kHz, and e) photopotential recorded for 50%w NTs by irradiating the sample with 340 nm monochromatic light.

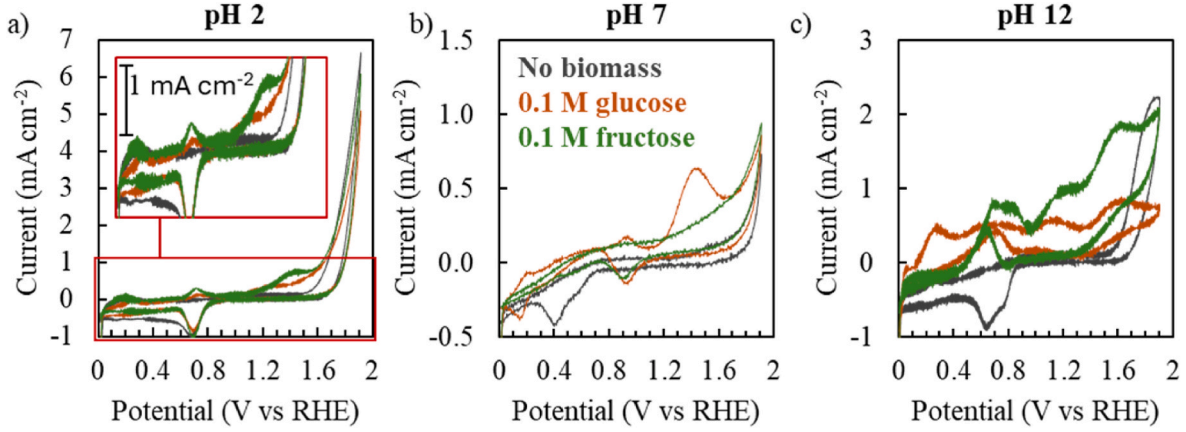

Fig. 5. Cyclic voltammetries carried out without irradiation by using Pt mesh as the counter and the working electrode, recorded at 5 mV/s in a 0.5 M Na_2SO_4 aqueous solution at a) pH 2, b) pH 7, and c) pH 12 with and without the presence of biomass.

The cyclic voltammograms recorded at pH 7 (Fig. 5b) show three peaks at 0.2, 0.9, and a more pronounced one at 1.4 V vs RHE only when glucose is present with the anodic current starting at 1.1 V vs RHE. According to the literature [62], the oxidation current at 0.2 V vs RHE is associated to the production of the carboxylic acids such as gluconic acid, glucuronic acid and/or glucaric acid with a higher selectivity towards the generation of gluconic acid. The reaction proceeds through a complex mechanism, in which at first step glucose is oxidized to gluconic acid, and when the potential is increased, gluconic acid generates CO species and cyclic carbonate, and both are practically completely removed from the electrode surface when they are oxidized to CO_2. According to the cyclic voltammogram recorded in biomass free solution, OER starts at ~1.5 V vs RHE. No peaks are observed with fructose, although an increased faradic current indicating its oxidation is noted by comparing the cyclic voltammetry recorded without and with fructose.

At pH 12 (Fig. 5c), the cyclic voltammograms show multiple peaks in presence of biomass, suggesting that several oxidation steps occur by increasing the applied potential involving oxidation of glucose or fructose. According to the literature [63,64] the first peak corresponds to the oxidation of the adsorbed hydrogen produced by glucose chemisorption, while peaks at 0.7 V vs RHE corresponds to the direct oxidation of glucose from the bulk. Finally, peak at 1.1 V vs RHE corresponds to the

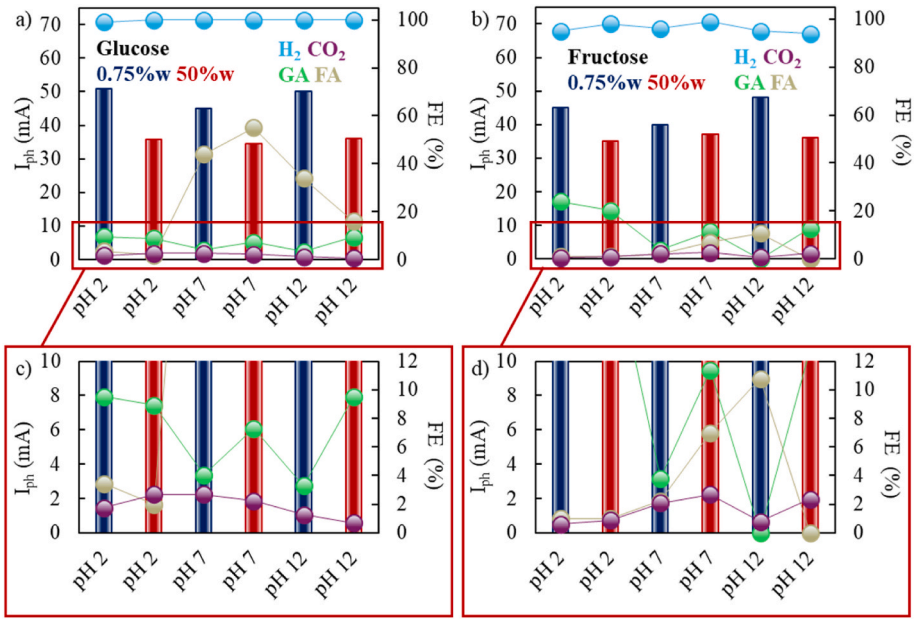

Fig. 6. Photoelectrochemical results obtained by using a) c) glucose or b) d) fructose as the starting biomass. The blue and red bars represent the photocurrent measured using the 0.75 wt% NTs and 50 wt% NTs samples, respectively. The calculated FEs are reported in the secondary axis for H_2 (turquoise), CO_2 (purple), gluconic acid (GA, green), and formic acid (FA, brown). The reaction time of each test was 3 h. (For interpretation of the references to colour in this figure legend, the reader is referred to the Web version of this article.)

oxidation of the adsorbed species resulting from the chemisorption of glucose occurring at lower potential. At this pH, OER appears to be partially inhibited in presence of fructose since water oxidation starts only at 1.7 V vs RHE, while with glucose there is no evidence of a current due to O_2 evolution up to 1.9 V vs RHE.

Fig. 6 summarizes the results of the photoelectrochemical reforming of glucose and fructose containing solutions at different pH (namely pH 2, 7 and 12), carried out under a bias of 1 V using the TiO_2 NTs photoanodes. First of all, it is important to stress that the measured photocurrent is comparable to that measured in biomass free solution (see Fig. S1a), but with higher hydrogen evolution rate due to the Faradic efficiency of 100% or slightly lower than 100 % for glucose and fructose containing solutions, respectively, in spite the use of undivided cell. Indeed, the amount of Oxygen produced at the photoanode is significantly lower, thus limiting the competition of O_2 reduction with respect to Hydrogen Evolution Reaction (HER). Moreover, I_{ph} is higher for NTs grown in solution with a low concentration of water, probably due to the higher thickness of the tubes' wall allowing a more efficient light absorption [55,65], but also to a more negative flat band potential with respect to NTs grown in 50%w solution. Indeed, the electric field driving the transport of photogenerated holes and electrons is directly connected to the band bending, $\Delta\Phi_{SC} = U_E - U_{FB}$ where U_E is the polarization potential [66]. Finally, for NTs grown with a low water concentration the measured photocurrent is slightly influenced by the electrolyte pH, the lowest value being measured in neutral solution. Conversely, the measured photocurrent is almost independent on the pH for TiO_2 NTs grown with a high concentration of water.

A clear idea of the products of the photoelectrochemical reactions is provided by the plots of Fig. 6, showing the faradic efficiencies for both the employed photoanodes as a function of the pH. For glucose, in acidic solution (pH = 2) the most abundant product is GA (FE ~ 8%) followed by FA and CO_2. This finding can be explained by CV recorded in the same solution (see Fig. 5a) showing very low current due to glucose oxidation and an onset potential for oxygen evolution close to the third oxidation step involving glucose.

Better results were obtained in neutral solution, where partial oxidation of glucose leads to a very high faradic efficiency in FA, even if FE for GA is lower than that measured at pH 2. At this pH according to the CV of Fig. 5b, the third glucose oxidation step occurs at potential significantly lower than that of O_2 evolution, which is therefore significantly less favourable on a kinetic point of view. At pH 12 the most favourable reaction is partial oxidation of glucose to FA, but with lower FE than that estimated at pH 7. These results were compared with those reported in the literature by normalizing the HVA and H_2 production rates based on the photoanode area and incident photon flux. To our knowledge, only one scientific article has been published on photoelectrochemical glucose reforming to obtain HVA and H_2 [37]. As shown in Table 3, our system demonstrated better performances in both cases, despite the use of PGM-free materials. Additionally, no scientific articles related to the photoelectrochemical oxidation of fructose to produce HVA have been found in the literature.

Table 3
Comparison with the literature of HVA and H_2 production rates normalized by photoanode area and incident photon flux.

	[37]	This work
Photoanode	Pt(SA)/def-TiO_2 NRs[a]	TiO_2 NTs
Cathode	Pt foil	Ni foam
Biomass	Glucose 0.01 M	Glucose 0.1 M
Electrolyte	1 M KOH	0.5 M Na_2SO_4 pH 7
Applied bias	0.6 V vs RHE	1 V (Cell potential)
Photoanode area (cm^2)	1	90
Light source (mW cm^{-2})	100	10
HVA production rate (μmol h^{-1} mW^{-1})	0.340[b]	0.565[c]
H_2 production rate (μmol h^{-1} mW^{-1})	0.356	0.933

[a] Defective TiO_2 nanorods decorated with Pt single atom.
[b] Considering both gluconic and glucaric acid.
[c] Considering both gluconic and formic acid.

Different results were obtained by photoelectrolysis of fructose containing solutions. At pH 2 the photoelectrochemical oxidation of the biomass leads to the formation of GA with FE = 24% and 20.3% for NTs grown in 0.75% water and 50% water, respectively. This finding agrees with the results of the cyclic voltammetry (see Fig. 5a) showing a better kinetic for fructose oxidation in acidic solution. Lower faradic

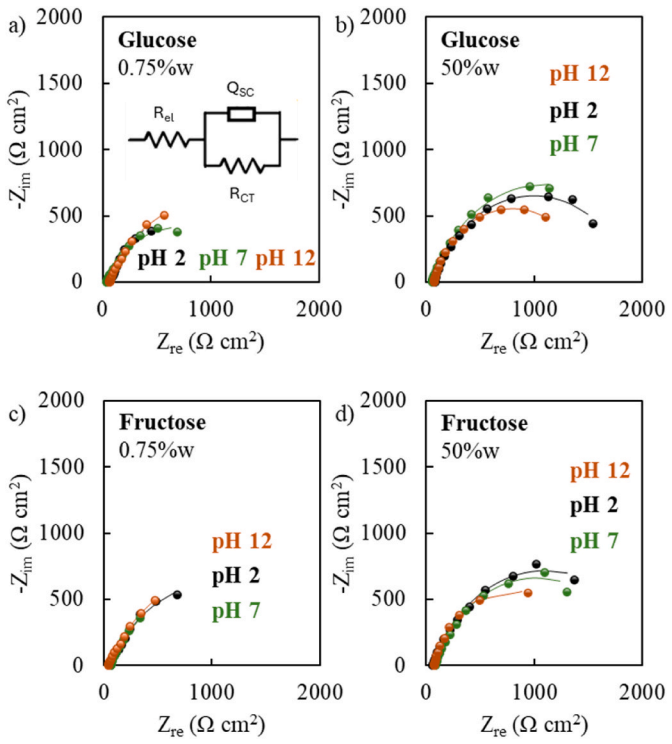

Fig. 7. In situ EIS spectra recorded under UV irradiation (125 W medium-pressure Hg lamp) in the presence of glucose a) – b) and fructose c) – d). All the spectra were fitted by using the equivalent circuit shown in the inset of a). Impedance spectra were measured within a frequency range of 100 kHz to 0.1 Hz, applying a potential of 1 V between the photoanode and cathode, and using an AC amplitude of 10 mV.

efficiencies for both GA and FA are estimated at higher pH, making the process less promising with respect to the photoelectrolysis of glucose.

Additionally, in the photoelectrocatalytic experiments that produced the highest FE towards FA and GA, quantum yields of 4.36% and 5.67% were calculated, respectively. More details can be found in the SI. However, it's important to note that, although this number is higher than typical values obtained in photocatalytic processes [3], a significant portion of the light is lost due to the cell geometry and, therefore, we are currently working on improving the cell design to minimize this energy loss.

Electrochemical impedance spectra were recorded under 1 V of bias during photoelectrolysis of both glucose and fructose. Fig. 7 shows the corresponding spectra in the Nyquist representation recorded under irradiation. For comparison we also recorded impedance spectra in biomass free solution (i.e. water photoelectrolysis) and without irradiation, that are reported in Figures S1 b-c and S2, with the relative fitting parameters in Tables S1–2. All the spectra are slightly depressed semicircles, thus they can be fitted with the very simple equivalent circuit of Fig. 7, where R_{CT} is the charge transfer resistance, Q_{SC} the capacitance of the semiconductor under irradiation, while R_{el} accounts for the electrolyte resistance. The corresponding fitting parameters are summarized in Table 4. At a first glance it is evident that a constant phase element is necessary to simulate the non-ideal capacitance of TiO_2 NTs layer (see exponent $n < 1$). Using the Brug formula [67] it is possible to estimate the NTs capacitance, that results slightly higher for NTs grown in solution with a lower concentration of water. This is in agreement with a higher concentration of donors as suggested by the more negative flat band potential measured for these NTs [36]. The higher doping level and the consequent higher concentration of charge carriers under irradiation explain the higher photocurrent measured for these NTs with respect to those grown in 50%water. Table 4 also reports the charge transfer resistance for both glucose and fructose oxidation at different pH and for both NTs layers. According to Table 4, the charge transfer resistance ranges from 1.3 to 2.3 kΩ cm^2, with the lowest value being measured during photoelectrolysis of glucose containing solution at pH 7 by employing 0.75%w NTs. Notably, it is interesting to mention that the charge transfer resistance is inversely proportional to the overall Faradic efficiency in biomass oxidation products due to the sluggish kinetic of oxygen evolution reaction affecting the overvoltage necessary to activate the reaction. The charge transfer resistances estimated in the presence of fructose are comparable to those estimated for glucose despite the lower photocurrent in agreement with a lower overall faradic efficiency and consequent higher photocurrent wasted for O_2.

4. Discussion

Fig. 8 shows the energetic of Ti/TiO_2 NTs/electrolyte interface.

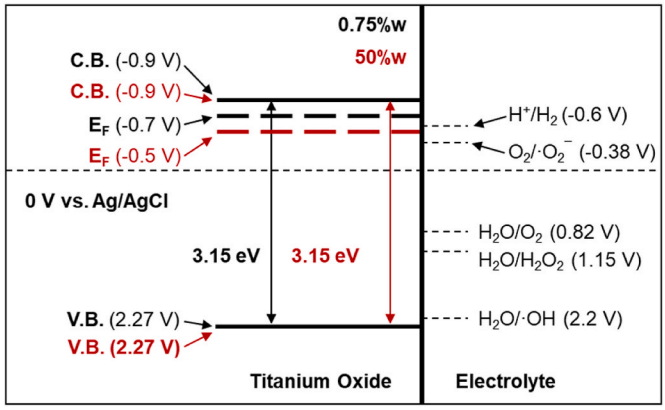

Fig. 8. Sketch of the energetic levels of the metal/oxide/electrolyte interface for the 0.75%w NTs sample (black) and 50%w NTs sample (red). (For interpretation of the references to colour in this figure legend, the reader is referred to the Web version of this article.)

Table 4
Fitting parameters obtained by EIS spectra recorded under irradiation.

Sample	pH	Substrate	R_{el} (Ω cm^2)	R_{CT} (Ω cm^2)	Q_{SC} (μS s^n cm^{-2})	n (adm)	C_{Brug} (μF cm^{-2})	χ square (adm)
0.75%w	2	Glucose	58	$2.3 \cdot 10^3$	$1.8 \cdot 10^{-3}$	0.68	622	$5.2 \cdot 10^{-3}$
50%w	2	Glucose	79	$1.8 \cdot 10^3$	$3.5 \cdot 10^{-4}$	0.79	135	$1.2 \cdot 10^{-3}$
0.75%w	2	Fructose	59	$2.0 \cdot 10^3$	$9.6 \cdot 10^{-4}$	0.71	297	$2.1 \cdot 10^{-3}$
50%w	2	Fructose	61	$2.1 \cdot 10^3$	$3.7 \cdot 10^{-4}$	0.77	119	$1.1 \cdot 10^{-3}$
0.75%w	7	Glucose	36	$1.3 \cdot 10^3$	$1.2 \cdot 10^{-3}$	0.72	354	$4.1 \cdot 10^{-3}$
50%w	7	Glucose	55	$2.1 \cdot 10^3$	$4.6 \cdot 10^{-4}$	0.78	163	$1.4 \cdot 10^{-3}$
0.75%w	7	Fructose	63	$1.7 \cdot 10^3$	$1.5 \cdot 10^{-3}$	0.73	627	$9.7 \cdot 10^{-4}$
50%w	7	Fructose	86	$1.9 \cdot 10^3$	$5.6 \cdot 10^{-4}$	0.78	238	$1.6 \cdot 10^{-3}$
0.75%w	12	Glucose	64	$1.8 \cdot 10^3$	$1.2 \cdot 10^{-3}$	0.75	510	$1.4 \cdot 10^{-3}$
50%w	12	Glucose	74	$1.5 \cdot 10^3$	$5.7 \cdot 10^{-4}$	0.82	284	$1.1 \cdot 10^{-3}$
0.75%w	12	Fructose	41	$2.4 \cdot 10^3$	$1.2 \cdot 10^{-3}$	0.69	310	$9.8 \cdot 10^{-4}$
50%w	12	Fructose	74	$1.4 \cdot 10^3$	$5.9 \cdot 10^{-4}$	0.84	325	$8.2 \cdot 10^{-4}$

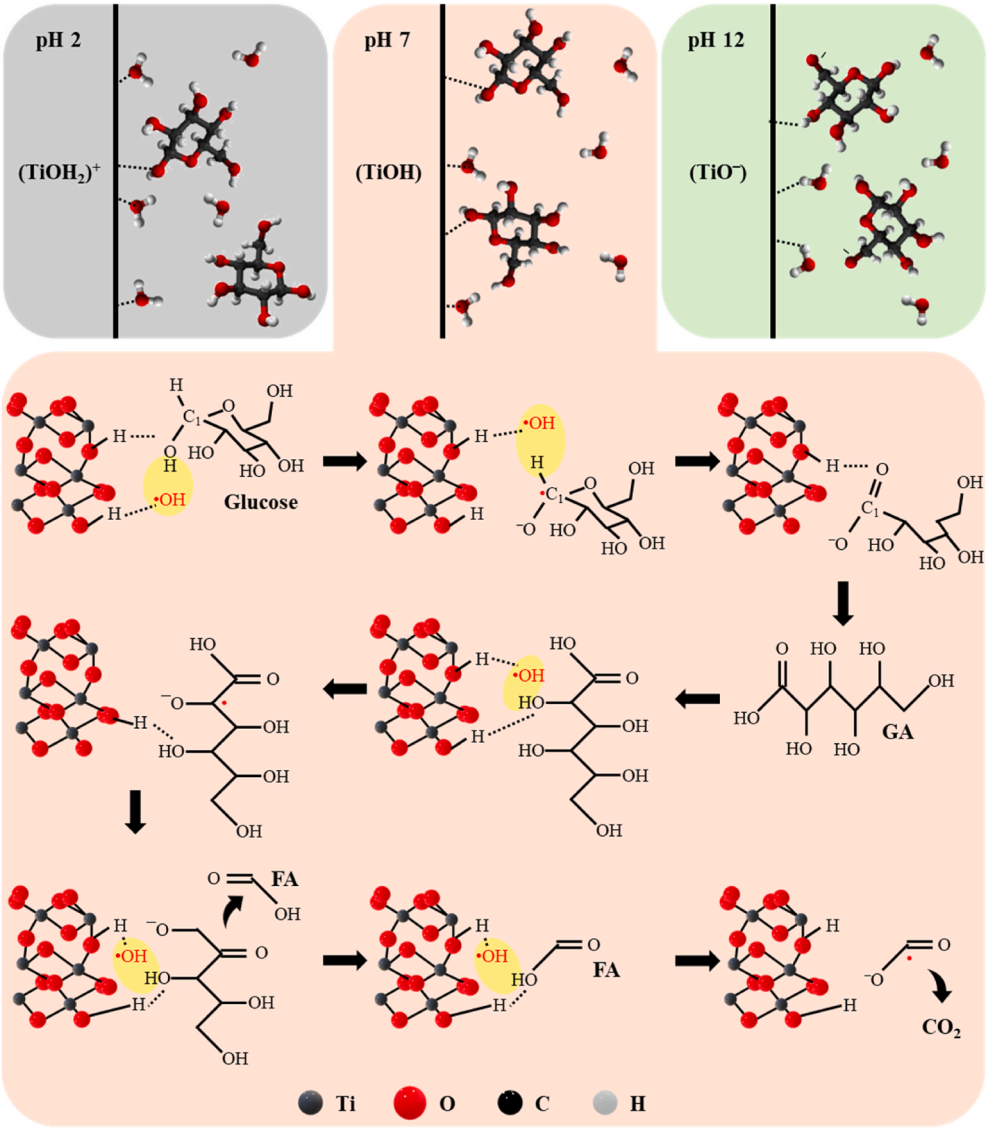

Fig. 9. Schematic illustration of interaction between NTs surface, water and glucose at various pH and the proposed reaction mechanism at pH 7.

Conduction and valence band edges were located according to the literature [36], while their flat band potential is quoted using the relationship reported in Equation (7):

$$E_F = -|e|\,U_{fb} + |e|\,U_{ref} \tag{7}$$

where U_{ref} represents the potential of the reference electrode used in the photoelectrochemical measurements.

According to this sketch, the photogenerated holes can oxidize water to produce not only oxygen and hydrogen peroxide, but also hydroxyl radicals. This information can be used to explain the reactions going on during biomass photoelectrolysis.

The results of glucose and fructose photoelectrolysis show that a proper selection of the process conditions allows to get high value added products with simultaneous hydrogen production. Carrying out the process at pH 7 in 0.1 M glucose aqueous solution allows to convert the biomass in formic acid with a good Faradic efficiency (44% and 55% for 0.75%w and 50%w NTs respectively) with part of the anodic current being also employed to produce gluconic acid. Hydrogen is produced at the cathode with a FE of 100%. Conversely, the best results starting with fructose containing solution are obtained at pH 2, where the reaction has a high selectivity toward gluconic acid whose production occurs with a Faradic efficiency of 24% and 20.3% for 0.75%w and 50%w NTs respectively.

These results suggest that glucose and fructose photoelectrochemical oxidation follows a different path. PEC oxidation of glucose to GA and FA on TiO_2 NTs photoanode starts with the generation of holes due to light absorption. The holes can oxidize water to form adsorbed •OH radicals, which in turn can oxidize the biomass (Fig. 8). According to previous results reported in the literature [4,16,37,68–72], a first adsorption step is necessary for biomass oxidation and, thus, the oxidation reaction rate as well as the products depend on how strong the biomass adsorption is (Fig. 9). The adsorption of glucose on TiO_2 surface is affected by the electrolyte pH, since the excess surface charge on TiO_2 depends on the pH of the solution with respect to the pH of zero charge, that for anodic TiO_2 is around 5.8 [73]. Surface hydroxyl groups are present on TiO_2 in aqueous solution, and they are involved in superficial ionization equilibria that can be described according to Equations (8) and (9):

$$-TiOH_2^+ \longleftrightarrow -TiOH + H^+ \tag{8}$$

$$-TiOH \longleftrightarrow -TiO^- + H^+ \tag{9}$$

where -TiOH represent an hydroxyl group on titanium oxide surface (i.e. titanol surface group). Thus, taking into account the pH of zero charge

for titania, we expect that the surface species are -$TiOH_2^+$ in acidic solution, -TiOH in neutral solution and -TiO− in alkaline conditions.

Glucose molecule (RHCOH) can be adsorbed on the catalyst through hydrogen bond (indicated as ···). The adsorption reaction can be expressed by Equation (10):

$$-TiOH + RHCOH \longleftrightarrow -TiOH\cdots OHCHR \quad (10)$$

As reported in Ref. [68], the pyranose oxygen of the cyclic form of glucose (Fig. 9) can strongly affect the hydroxyl group at C_1 due to the shortest distance, therefore the strength of hydrogen bond between -TiOH and the hydroxyl group at C_1 is much larger than those between -TiOH and other hydroxyl groups. Thus, we could assume that a glucose molecule can be adsorbed mainly at TiO_2 surface by the hydroxyl group at C_1. As soon as irradiation generates electron-hole pairs, electrons are transported by the electric field (due to the band bending) toward the cathode through the external circuit where they allow HER. The holes in the valence band can oxidize water to produce hydroxyl radicals on the TiO_2 surface, i.e. $TiOH^+\cdot$. Adsorbed glucose (electron donor) is oxidized by these species at C_1, as shown in Equation (11):

$$-TiOH\bullet + RHCOH \longleftrightarrow -TiOH_2^+ + RC\bullet OH \quad (11)$$

The formed RC•OH can react further with water and the hydroxyl radicals to produce GA. Subsequently, the C_5–O bond is split by hydrolysis, and then the GA is formed through desorption from the photoanode in agreement with previous findings reported in the literature [37]. Gluconic acid would react further with hydroxyl radicals so that C_5 compounds with formic acid are formed. Since there is no evidence of C_5 compounds among the products, these compounds are presumably converted to C_4 compounds by the further attack of radicals, followed by the formation of C_3 compounds, and so on. Finally, carbon dioxide may be the mineralization product for the photoelectrocatalytic degradation of glucose explaining the presence of only GA, FA and CO_2.

Notably, the fraction of titania where glucose is adsorbed depends on the pH due to effect on the excess charge on titania surface as well as on the possibility to find glucose in ionic form. Indeed, pKa of glucose is about 12.3 [72]. When the pH < pKa, glucose in the solution is mainly in molecular form, while in alkaline condition, it can dissociate into $RHCO^-$, which can be adsorbed on TiO_2 through hydrogen bonds. Due to the negative charge of the dissociated form, $RHCO^-$ captures holes more efficiently than the molecular form. However, with increasing pH the surface of titania is negatively charged, hence electrostatic repulsion between TiO^- and $RHCO^-$ increases slowing down the formation rate of glucose oxidation products. This explains why the highest faradic efficiency of glucose oxidation is measured at pH 7, i.e. in a neutral solution not so far from the pH of zero charge.

A different behaviour is observed with fructose that shows the highest faradic efficiency in products other than oxygen at pH 2. It is likely that the adsorption of fructose on TiO_2 surface is weaker than that of glucose in agreement with DFT calculation of the adsorption energy for both sugars [71] with a negative impact on the kinetic of fructose oxidation.

5. Conclusions

Photoelectrochemical H_2 and HVA production in PGM-free cells via glucose and fructose photo-oxidation at various pH was investigated using TiO_2 nanotubes on Ti felt with different features as the photoanode and Ni foam as the cathode, with working areas of 90 cm^2 and 180 cm^2, respectively. Photoelectrocatalytic tests in biomass containing solutions showed that their presence enhanced the H_2 production rate up to 0.933 μmol h^{-1} mW^{-1} and ~100% of faradic efficiency (FE), with the formation of valuable oxidation products such as gluonic acid and formic acid up to 0.565 μmol h^{-1} mW^{-1} and FE of 25% and 55% respectively.

Notably, this study demonstrated that the PEC oxidation of glucose and fructose using TiO_2 NT photoanodes is a promising approach for producing hydrogen and high-value-added chemicals under mild conditions. The findings highlight the importance of optimizing NTs synthesis conditions and pH reaction medium to enhance PEC performance and product selectivity. Moreover, both the photoanode and cathode demonstrated high mechanical and chemical stability, allowing reusability under the reaction conditions.

CRediT authorship contribution statement

Claudio M. Pecoraro: Writing – original draft, Visualization, Investigation. **Francesco Di Franco:** Writing – review & editing, Visualization. **Vittorio Loddo:** Writing – review & editing. **Marianna Bellardita:** Writing – review & editing, Supervision, Conceptualization. **Monica Santamaria:** Writing – review & editing, Supervision, Funding acquisition, Conceptualization.

Declaration of competing interest

The authors declare that they have no known competing financial interests or personal relationships that could have appeared to influence the work reported in this paper.

Acknowledgements

C.M.P. acknowledges support from the University of Palermo.

Appendix A. Supplementary data

Supplementary data to this article can be found online at https://doi.org/10.1016/j.ijhydene.2024.09.124.

References

[1] Zhang L, Jia C, Bai F, Wang W, An S, Zhao K, et al. A comprehensive review of the promising clean energy carrier: hydrogen production, transportation, storage, and utilization (HPTSU) technologies. Fuel 2024;355:129455. https://doi.org/10.1016/J.FUEL.2023.129455.

[2] Hosseini SE, Wahid MA. Hydrogen from solar energy, a clean energy carrier from a sustainable source of energy. Int J Energy Res 2020;44:4110–31. https://doi.org/10.1002/ER.4930.

[3] Pecoraro CM, Bellardita M, Loddo V, Virtù D, Di Franco F, Santamaria M. Photocatalytic and photoelectrocatalytic H_2 evolution combined with valuable furfural production. Appl Catal Gen 2023;650:118987. https://doi.org/10.1016/j.apcata.2022.118987.

[4] Bellardita M, García-López EI, Marcì G, Palmisano L. Photocatalytic formation of H_2 and value-added chemicals in aqueous glucose (Pt)-TiO_2 suspension. Int J Hydrogen Energy 2016;41:5934–47. https://doi.org/10.1016/J.IJHYDENE.2016.02.103.

[5] Yu IKM, Ong KL, Tsang DCW, Haque MA, Kwan TH, Chen SS, et al. Chemical transformation of food and beverage waste-derived fructose to hydroxymethylfurfural as a value-added product. Catal Today 2018;314:70–7. https://doi.org/10.1016/J.CATTOD.2018.01.011.

[6] Lee J, Jung S, Kim YT, Kim HJ, Kim KH. Catalytic and electrocatalytic conversion of glucose into value-added chemicals. Renew Sustain Energy Rev 2023;181:113337. https://doi.org/10.1016/J.RSER.2023.113337.

[7] Aboagye D, Djellabi R, Medina F, Contreras S. Radical-mediated photocatalysis for lignocellulosic biomass conversion into value-added chemicals and hydrogen: facts, opportunities and challenges. Angew Chem 2023;135:e202301909. https://doi.org/10.1002/ANGE.202301909.

[8] Awasthi MK, Sar T, Gowd SC, Rajendran K, Kumar V, Sarsaiya S, et al. A comprehensive review on thermochemical, and biochemical conversion methods of lignocellulosic biomass into valuable end product. Fuel 2023;342:127790. https://doi.org/10.1016/J.FUEL.2023.127790.

[9] Deng W, Zhang Q, Wang Y. Catalytic transformations of cellulose and cellulose-derived carbohydrates into organic acids. Catal Today 2014;234:31–41. https://doi.org/10.1016/j.cattod.2013.12.041.

[10] Olivito F, Algieri V, Tallarida MA, Jiritano A, Costanzo P, Maiuolo L, et al. High-yield synthesis of HMF from glucose and fructose by selective catalysis with water-tolerant rare earth metal triflates assisted by choline chloride. Green Chem 2023;25:1679–89. https://doi.org/10.1039/D2GC04046H.

[11] Zhang S, Sun J, Feng D, Sun H, Cui J, Zeng X, et al. Unlocking the potentials of cyanobacterial photosynthesis for directly converting carbon dioxide into glucose. Nat Commun 2023;14(1 2023;14):1–14. https://doi.org/10.1038/s41467-023-39222-w.

[12] Hwang KR, Jeon W, Lee SY, Kim MS, Park YK. Sustainable bioplastics: recent progress in the production of bio-building blocks for the bio-based next-generation

polymer PEF. Chem Eng J 2020;390:124636. https://doi.org/10.1016/J.CEJ.2020.124636.
[13] Shinde S, Tarade K, Mitra G, Rode C. Integration of heterogeneous acid and base catalysis for clean synthesis of jet-fuel precursor from carbohydrates. ChemistrySelect 2020;5:392–400. https://doi.org/10.1002/SLCT.201903735.
[14] Alamgir Ahmad K, Haider Siddiqui M, Pant KK, Nigam KDP, Shetti NP, Aminabhavi TM, et al. A critical review on suitability and catalytic production of butyl levulinate as a blending molecule for green diesel. Chem Eng J 2022;447:137550. https://doi.org/10.1016/J.CEJ.2022.137550.
[15] Karádi K, Nguyen TT, Ádám AA, Baán K, Sápi A, Kukovecz Á, et al. Structure–activity relationships of LDH catalysts for the glucose-to-fructose isomerisation in ethanol. Green Chem 2023;25:5741–55. https://doi.org/10.1039/D3GC01860A.
[16] Bellardita M, García-López EI, Marcì G, Nasillo G, Palmisano L. Photocatalytic solar light H_2 production by aqueous glucose reforming. Eur J Inorg Chem 2018;2018:4522–32. https://doi.org/10.1002/ejic.201800663.
[17] Guo H, Li J, Xu S, Yang J, Chong GH, Shen F. Mo-modified MnOx for the efficient oxidation of high-concentration glucose to formic acid in water. Fuel Process Technol 2023;242:107662. https://doi.org/10.1016/J.FUPROC.2023.107662.
[18] Álvarez-Hernández D, Ivanova S, Penkova A, Centeno MÁ. Influence of vanadium species on the catalytic oxidation of glucose for formic acid production. Catal Today 2024;441:114906. https://doi.org/10.1016/J.CATTOD.2024.114906.
[19] Xia T, Ju M, Qian H, Bai X, Lai R, Xie C, et al. Photocatalytic fenton-like system with atomic Fe on carbon nitride boost selective glucose oxidation towards gluconic acid. J Catal 2024;429:115257. https://doi.org/10.1016/J.JCAT.2023.115257.
[20] Wang J, Chen L, Zhao H, Kumar P, Larter SR, Kibria MG, et al. In situ photo-fenton-like tandem reaction for selective gluconic acid production from glucose photo-oxidation. ACS Catal 2023;13:2637–46. https://doi.org/10.1021/ACSCATAL.2C05931.
[21] Ramachandran S, Fontanille P, Pandey A, Larroche C. Gluconic acid: properties, applications and microbial production. Food Technol Biotechnol 2006;44:185–95.
[22] Machado JV, da Silva MLA, Silva CLS, Correia MCG, da Silva Ruy AD, Pontes LAM. Catalysts and processes for gluconic and glucaric acids production: a comprehensive review of market and chemical routes. Catal Commun 2023;182:106740. https://doi.org/10.1016/J.CATCOM.2023.106740.
[23] Chen Y, Yang Y, Liu X, Shi X, Wang C, Zhong H, et al. Sustainable production of formic acid and acetic acid from biomass. Mol Catal 2023;545:113199. https://doi.org/10.1016/J.MCAT.2023.113199.
[24] Wasik DO, Martín-Calvo A, Gutiérrez-Sevillano JJ, Dubbeldam D, Vlugt TJH, Calero S. Enhancement of formic acid production from carbon dioxide hydrogenation using metal-organic frameworks: Monte Carlo simulation study. Chem Eng J 2023;467:143432. https://doi.org/10.1016/J.CEJ.2023.143432.
[25] Deng W, Feng Y, Fu J, Guo H, Guo Y, Han B, et al. Catalytic conversion of lignocellulosic biomass into chemicals and fuels. Green Energy Environ 2023;8:10–114. https://doi.org/10.1016/J.GEE.2022.07.003.
[26] Zhang H, Yang K, Tao Y, Yang Q, Xu L, Liu C, et al. Biomass directional pyrolysis based on element economy to produce high-quality fuels, chemicals, carbon materials – a review. Biotechnol Adv 2023;69:108262. https://doi.org/10.1016/J.BIOTECHADV.2023.108262.
[27] Zhang B, Biswal BK, Zhang J, Balasubramanian R. Hydrothermal treatment of biomass feedstocks for sustainable production of chemicals, fuels, and materials: progress and perspectives. Chem Rev 2023;123:7193–294. https://doi.org/10.1021/ACS.CHEMREV.2C00673/ASSET/IMAGES/MEDIUM/CR2C00673_0046.GIF.
[28] Yun J, Yao G, Jin F, Zhong H, Kishita A, Tohji K, et al. Low-temperature and highly efficient conversion of saccharides into formic acid under hydrothermal conditions. AIChE J 2016;62:3657–63. https://doi.org/10.1002/AIC.15287.
[29] Wang C, Chen X, Qi M, Wu J, Gözaydin G, Yan N, et al. Room temperature, near-quantitative conversion of glucose into formic acid. Green Chem 2019;21:6089–96. https://doi.org/10.1039/C9GC02201E.
[30] Liu A, Huang Z, Wang X. Efficient oxidation of glucose into gluconic acid catalyzed by oxygen-rich carbon supported Pd under room temperature and atmospheric pressure. Catal Letters 2018;148:2019–29. https://doi.org/10.1007/S10562-018-2409-1/TABLES/5.
[31] Onda A, Ochi T, Kajiyoshi K, Yanagisawa K. A new chemical process for catalytic conversion of d-glucose into lactic acid and gluconic acid. Appl Catal Gen 2008;343:49–54. https://doi.org/10.1016/J.APCATA.2008.03.017.
[32] Yu FY, Zhou YJ, Tan HQ, Li YG, Kang ZH. Versatile photoelectrocatalysis strategy raising up the green production of hydrogen peroxide. Adv Energy Mater 2023;13:2300119. https://doi.org/10.1002/AENM.202300119.
[33] Li P, Liu Y, Mushtaq MA, Yan D. Recent progress in ammonia synthesis based on photoelectrocatalysis. Inorg Chem Front 2023;10:4650–67. https://doi.org/10.1039/D3QI00683B.
[34] Feng X, Feng X, Zhang F. Enhanced photoelectrochemical oxidation of glycerol to dihydroxyacetone coupled with hydrogen generation via accelerative middle hydroxyl dehydrogenation over a Bi^0/Bi^{3+} interface of a cascade heterostructure. J Mater Chem A Mater 2023;11:20242–53. https://doi.org/10.1039/D3TA04326F.
[35] Yu J, González-Cobos J, Dappozze F, Vernoux P, Caravaca A, Guillard C. Basic comprehension and recent trends in photoelectrocatalytic systems. Green Chem 2024;26:1682–708. https://doi.org/10.1039/D3GC03371F.
[36] Pecoraro CM, Di Franco F, Bellardita M, Loddo V, Santamaria M. Enhancing H_2 production rate in PGM-free photoelectrochemical cells by glycerol photo-oxidation. Int J Hydrogen Energy 2024;49:322–36. https://doi.org/10.1016/j.ijhydene.2023.08.011.
[37] Tian Z, Da Y, Wang M, Dou X, Cui X, Chen J, et al. Selective photoelectrochemical oxidation of glucose to glucaric acid by single atom Pt decorated defective TiO_2. Nat Commun 2023;14(1 2023;14):1–12. https://doi.org/10.1038/s41467-023-35875-9.
[38] Tryk DA, Fujishima A, Honda K. Recent topics in photoelectrochemistry: achievements and future prospects. Electrochim Acta 2000;45:2363–76. https://doi.org/10.1016/S0013-4686(00)00337-6.
[39] Tan MX, Laibinis PE, Nguyen ST, Kesselman JM, Stanton CE, Lewis NS. Principles and applications of semiconductor photoelectrochemistry. Prog Inorg Chem 2007;41:21–144. https://doi.org/10.1002/9780470166420.CH2.
[40] Grätzel M. Photoelectrochemical cells. Nature 2001;414:338–44.
[41] Pitchaimuthu S, Sridharan K, Nagarajan S, Ananthraj S, Robertson P, Kuehnel MF, et al. Solar hydrogen fuel generation from wastewater—beyond photoelectrochemical water splitting: a perspective. Energies 2022;15. https://doi.org/10.3390/EN15197399.
[42] Li YH, Zhang F, Chen Y, Li JY, Xu YJ. Photoredox-catalyzed biomass intermediate conversion integrated with H2 production over Ti3C2Tx/CdS composites. Green Chem 2020;22:163–9. https://doi.org/10.1039/C9GC03332G.
[43] Kumar MP, Jagannathan R, Ravichandran S. Photoelectrochemical system for unassisted high-efficiency water-splitting reactions using N-doped TiO2Nanotubes. Energy Fuel 2020;34:9030–6. https://doi.org/10.1021/ACS.ENERGYFUELS.0C00634.
[44] Govind Rajan A, Martirez JMP, Carter EA. Why do we use the materials and operating conditions we use for heterogeneous (Photo)Electrochemical water splitting? ACS Catal 2020;10. https://doi.org/10.1021/ACSCATAL.0C01862.
[45] Yao T, An X, Han H, Chen JQ, Li C. Photoelectrocatalytic materials for solar water splitting. Adv Energy Mater 2018;8:1800210. https://doi.org/10.1002/AENM.201800210.
[46] Chen W, Liu S, Fu Y, Yan H, Qin L, Lai C, et al. Recent advances in photoelectrocatalysis for environmental applications: sensing, pollutants removal and microbial inactivation. Coord Chem Rev 2022;454:214341. https://doi.org/10.1016/J.CCR.2021.214341.
[47] Brillas E, Garcia-Segura S. Recent progress of applied TiO2 photoelectrocatalysis for the degradation of organic pollutants in wastewaters. J Environ Chem Eng 2023;11:109635. https://doi.org/10.1016/j.jece.2023.109635.
[48] Alulema-Pullupaxi P, Espinoza-Montero PJ, Sigcha-Pallo C, Vargas R, Fernández L, Peralta-Hernández JM, et al. Fundamentals and applications of photoelectrocatalysis as an efficient process to remove pollutants from water: a review. Chemosphere 2021;281:130821. https://doi.org/10.1016/J.CHEMOSPHERE.2021.130821.
[49] Yu J, González-Cobos J, Dappozze F, Grimaldos-Osorio N, Vernoux P, Caravaca A, et al. First PEM photoelectrolyser for the simultaneous selective glycerol valorization into value-added chemicals and hydrogen generation. Appl Catal, B 2023;327:122465. https://doi.org/10.1016/J.APCATB.2023.122465.
[50] Shi Q, Duan H. Recent progress in photoelectrocatalysis beyond water oxidation. Chem Catal 2022;2:3471–96. https://doi.org/10.1016/j.checat.2022.11.007.
[51] Yurdakal S, Alagöz O, Özcan L, Palmisano L. Selective photoelectrocatalytic transformations of organic compounds. Photoelectrocatalysis: Fundamentals and Applications 2023:361–420. https://doi.org/10.1016/B978-0-12-823989-6.00001-1.
[52] Bellardita M, Yurdakal S, Tek BS, Değirmenci Ç, Palmisano G, Loddo V, et al. Tuning the selectivity to aldehyde via pH regulation in the photocatalytic oxidation of 4-methoxybenzyl alcohol and vanillyl alcohol by TiO2 catalysts. J Environ Chem Eng 2021;9:105308. https://doi.org/10.1016/j.jece.2021.105308.
[53] Di Paola A, Bellardita M, Palmisano L, Barbieriková Z, Brezová V. Influence of crystallinity and OH surface density on the photocatalytic activity of TiO2 powders. J Photochem Photobiol Chem 2014:59–67. https://doi.org/10.1016/J.JPHOTOCHEM.2013.09.008. Complete.
[54] Wang Y, Zu M, Zhou X, Lin H, Peng F, Zhang S. Designing efficient TiO2-based photoelectrocatalysis systems for chemical engineering and sensing. Chem Eng J 2020;381:122605. https://doi.org/10.1016/J.CEJ.2019.122605.
[55] Roy P, Berger S, Schmuki P. TiO2 nanotubes: synthesis and applications. Angew Chem Int Ed 2011;50:2904–39. https://doi.org/10.1002/anie.201001374.
[56] Kowalski D, Kim D, Schmuki P. TiO2 nanotubes, nanochannels and mesosponge: self-organized formation and applications. Nano Today 2013;8:235–64. https://doi.org/10.1016/j.nantod.2013.04.010.
[57] Santamaria M, Conigliaro G, Di Franco F, Di Quarto F. Photoelectrochemical evidence of Cu2O/TiO2Nanotubes hetero-junctions formation and their physicochemical characterization. Electrochim Acta 2014;144:315–23. https://doi.org/10.1016/j.electacta.2014.07.154.
[58] Reyes-Coronado D, Rodríguez-Gattorno G, Espinosa-Pesqueira ME, Cab C, de Coss R, Oskam G. Phase-pure TiO $_2$ nanoparticles: anatase, brookite and rutile. Nanotechnology 2008;19:145605. https://doi.org/10.1088/0957-4484/19/14/145605.
[59] Balachandran U, Eror NG. Raman spectra of titanium dioxide. J Solid State Chem 1982;42:276–82. https://doi.org/10.1016/0022-4596(82)90006-8.
[60] Pecoraro CM, Bellardita M, Loddo V, Di Franco F, Palmisano L, Santamaria M. A facile way to synthesize noble metal free TiO2 based catalysts for glycerol photoreforming. J Ind Eng Chem 2023;118:247–58. https://doi.org/10.1016/j.jiec.2022.11.010.
[61] Bae IT, Xing X, Liu CC, Yeager E. In situ Fourier transform infrared reflection absorption spectroscopic studies of glucose oxidation on platinum in acid, vol. 284. Sequoia S.A: Elsevier; 1990.
[62] Mello GAB, Cheuquepán W, Briega-Martos V, Feliu JM. Glucose electro-oxidation on Pt(100) in phosphate buffer solution (pH 7): a mechanistic study. Electrochim Acta 2020;354. https://doi.org/10.1016/j.electacta.2020.136765.

[63] Moggia G, Kenis T, Daems N, Breugelmans T. Electrochemical oxidation of <scp>d</scp> -glucose in alkaline medium: impact of oxidation potential and chemical side reactions on the selectivity to d-gluconic and d-glucaric acid. Chemelectrochem 2020;7:86–95. https://doi.org/10.1002/celc.201901592.
[64] Faverge T, Gilles B, Bonnefont A, Maillard F, Coutanceau C, Chatenet M. In situ investigation of d-glucose oxidation into value-added products on Au, Pt, and Pd under alkaline conditions: a comparative study. ACS Catal 2023;13:2657–69. https://doi.org/10.1021/acscatal.2c05871.
[65] Lee K, Mazare A, Schmuki P. One-dimensional titanium dioxide nanomaterials: nanotubes. Chem Rev 2014;114:9385–454. https://doi.org/10.1021/CR500061M/ASSET/IMAGES/MEDIUM/CR-2014-00061M_0039. GIF.
[66] La Mantia F, Stojadinović J, Santamaria M, Di Quarto F. Dynamic response of thin-film semiconductors to AC voltage perturbations. ChemPhysChem 2012;13:2910–8. https://doi.org/10.1002/CPHC.201200226.
[67] Hirschorn B, Orazem ME, Tribollet B, Vivier V, Frateur I, Musiani M. Determination of effective capacitance and film thickness from constant-phase-element parameters. Electrochim Acta 2010;55:6218–27. https://doi.org/10.1016/j.electacta.2009.10.065.
[68] Lan L, Daly H, Sung R, Tuna F, Skillen N, Robertson PKJ, et al. Mechanistic study of glucose photoreforming over TiO2-based catalysts for H2 production. ACS Catal 2023;13:8574–87. https://doi.org/10.1021/acscatal.3c00858.
[69] Shi C, Eqi M, Shi J, Huang Z, Qi H. Constructing 3D hierarchical TiO2 microspheres with enhanced mass diffusion for efficient glucose photoreforming under modulated reaction conditions. J Colloid Interface Sci 2023;650:1736–48. https://doi.org/10.1016/j.jcis.2023.07.081.
[70] Zhu Y, Tan R, Yang C, Zhang B, Deng K, Tang D, et al. Efficient visible light photocatalytic performance of bismuth trioxide/titanium dioxide composite for selective conversion of glucose to arabinose and formic acid. Mol Catal 2024;554. https://doi.org/10.1016/j.mcat.2024.113818.
[71] Ding Y, Cao Y, Chen D, Li J, Wu H, Meng Y, et al. Relay photo/thermal catalysis enables efficient cascade upgrading of sugars to lactic acid: mechanism study and life cycle assessment. Chem Eng J 2023;452. https://doi.org/10.1016/j.cej.2022.139687.
[72] Zhou M, Li Y, Peng S, Lu G, Li S. Effect of epimerization of d-glucose on photocatalytic hydrogen generation over Pt/TiO_2. Catal Commun 2012;18:21–5. https://doi.org/10.1016/j.catcom.2011.11.017.
[73] Bubacz K, Tryba B, Morawski AW. The role of adsorption in decomposition of dyes on TiO_2 and N-modified TiO_2 photocatalysts under UV and visible light irradiations. Mater Res Bull 2012;47:3697–703. https://doi.org/10.1016/J.MATERRESBULL.2012.06.038.